Journal of
Biomedical Optics

BiomedicalOptics.SPIEDigitalLibrary.org

Contrast improvement of continuous wave diffuse optical tomography reconstruction by hybrid approach using least square and genetic algorithm

Rusha Patra
Pranab K. Dutta

SPIE.

Journal of Biomedical Optics 20(7), 075009 (July 2015)

Contrast improvement of continuous wave diffuse optical tomography reconstruction by hybrid approach using least square and genetic algorithm

Rusha Patra* **and Pranab K. Dutta**
Indian Institute of Technology Kharagpur, Department of Electrical Engineering, Kharagpur, West Bengal 721302, India

Abstract. Reconstruction of the absorption coefficient of tissue with good contrast is of key importance in functional diffuse optical imaging. A hybrid approach using model-based iterative image reconstruction and a genetic algorithm is proposed to enhance the contrast of the reconstructed image. The proposed method yields an observed contrast of 98.4%, mean square error of 0.638×10^{-3}, and object centroid error of (0.001 to 0.22) mm. Experimental validation of the proposed method has also been provided with tissue-like phantoms which shows a significant improvement in image quality and thus establishes the potential of the method for functional diffuse optical tomography reconstruction with continuous wave setup. A case study of finger joint imaging is illustrated as well to show the prospect of the proposed method in clinical diagnosis. The method can also be applied to the concentration measurement of a region of interest in a turbid medium. [DOI: 10.1117/1.JBO.20.7.075009]

Keywords: diffuse optical tomography; image reconstruction; nonlinear regularized least square; genetic algorithm.

Paper 150057R received Jan. 30, 2015; accepted for publication Jun. 29, 2015; published online Jul. 29, 2015.

1 Introduction

Over the last few decades, there has been considerable research on optical imaging. The basic principle involves the transillumination of a tissue using a near-infrared (NIR) light source and the reconstruction of the optical properties (such as optical absorption, scattering, and so on) from the intensity measurements along the boundary. One of the main focuses of these studies is that in the NIR range, the depth of penetration is moderate and the absorption coefficient changes with concentration of different tissue constituents like hemoglobin, water, protein, fat, and so on. Hence, a mapping of these features can be inferred from the reconstructed absorption coefficient, though it is qualitative in many cases. In diffuse optical tomography (DOT), the photon diffusion in the medium is modeled and the optical properties of the medium are reconstructed from the measurements at the boundary. Some potential applications of DOT includes brain imaging,[1] breast tumor detection,[2] monitoring the condition of finger joints,[3] and so on. It is evident from the basic principle that DOT is generally an ill-posed and underdetermined imaging problem. As the photons are diffused in the tissue at NIR, DOT is capable of imaging a larger volume. At the same time, due to the high scattering of photons, the inverse problem of DOT is nonlinear. These factors lead to theoretical as well as practical difficulties in finding a unique and reliable solution. Various approaches for DOT exist depending on the measurement type, source-detector arrangement, and image reconstruction algorithm. Extensive studies have been carried out on frequency and time domain DOT. However, these require sophisticated hardware, a large time for data acquisition, and high cost. In this study, continuous wave (CW) measurement with transmittance geometry is considered. CW measurement employs CW light sources, simple detectors like photodiodes, and so on, which make the setup simple and of low cost. The image quality of CWDOT depends on the source-detector density, whereas frequency domain DOT has medium image quality and time domain DOT has the highest image quality. Therefore, in the present study, the improvement of the image quality of CWDOT has been considered. The reconstruction of the absorption coefficient is focused only with a known scattering coefficient.

Solution of the DOT inverse problem was reported first in 1993. An iterative image recovery algorithm has been proposed where the forward problem was solved by using finite element method.[4] The advances in the reconstruction as well as instrumentation in the last two decades have been summarized in the review article by Arridge and Schotland.[5] The nonlinear inverse problem can be linearized by expansion and approximation, where the functional relationship between the measurements and the inputs is approximated as a sparse matrix. Due to sparsity of the linearized inverse problem, compressed sensing,[6] and different variant of MUSIC algorithms[7] have been applied for DOT reconstruction. Use of neural network for DOT reconstruction has been reported as well.[8] Though these methods provide acceptable spatial accuracy and resolution, the reconstructed absorption coefficients are not always quantitatively the same as the actual one resulting in a low-contrast reconstructed image. The contrast is extremely important in functional DOT for the mapping of the absorption coefficient to the concentration of oxygenated and deoxygenated hemoglobin. Recently, contrast improvement of the CW-DOT reconstruction using ℓ_p norm[9,10] or basis pursuit deconvolution[11] has been reported as well. In Ref. 9, a linearized ℓ_1-based framework has been provided for dynamic CW-DOT, whereas in Ref. 10, a systematic comparison of different ℓ_p $(0 < p < 1)$ minimization

---

*Address all correspondence to: Rusha Patra, Email: rusha.ee@iitkgp.ac.in

1083-3668/2015/$25.00 © 2015 SPIE

algorithms are discussed for DOT imaging. In Ref. 11, CW-DOT image reconstruction is improved by using basic pursuit deconvolution. Along with the conventional optimization methods, evolutionary algorithms like the genetic algorithm (GA) are also used in DOT reconstruction. GA has been introduced for estimating the optical properties of homogenous media[12–14] where the number of unknowns is only 3 (global absorption and scattering coefficients, and anisotropy factor). For heterogeneous media, the number of unknowns will be of the order of the total number of finite elements which leads to highly expensive computations. The use of GA for reconstructing heterogeneity has been reported in Refs. 15 and 16. In Ref. 15, the absorption coefficient is considered as a Gaussian shaped perturbation and only a single inclusion is considered, which can include only a few special cases. In Ref. 16, both single and double inclusions are considered for reconstruction. However, the number of inhomogeneities is assumed to be known in the simulation results. This has been shown as the proof of convergence of GA onto a good solution. A two-step approach that takes advantage of both global optimization and gradient techniques to solve the DOT inverse problem has been shown in Ref. 17. The method utilizes the fitted values of the unknown target parameters estimated from GA as the initial values for the conjugate gradient reconstruction. Prior to imaging, the desired area was examined using ultrasonography (USG) and the locations of inclusions (mean and standard deviation) are computed from B-scan images of USG. Here, usage of another imaging modality and detection circuit of the frequency domain DOT system makes the instrument expensive.

Considering all these limitations, a hybrid approach using both the gradient based technique and evolutionary method is proposed here for CW-DOT reconstruction. The main objective is to reconstruct the region of absorption heterogeneities in a nearly homogeneous background with accurate spatial location as well as absorption coefficient values. In the proposed hybrid approach, the absorption coefficients are initially reconstructed using a regularized least square method, then the reconstructed coefficients of the region of heterogeneities are refined using GA. The performance of the proposed method has been assessed quantitatively and also compared with those of existing methods. A comprehensive experimentation has also been carried out with a tissue-like phantom to validate the proposed method. Significant improvement of image quality is achieved, which indicates the potential of the proposed method in functional imaging. Finally, imaging of a transverse section of human index distal interphalangeal (DIP) is demonstrated as an example of clinical application for detecting osteoarthritis (OA).

The organization of this paper is as follows. In Sec. 2, optical characteristics of tissue as well as photon propagation and proposed DOT image reconstruction are described. Experimental setup and phantom preparation are described in Sec. 3. Simulation, experimental as well as DIP imaging results, and comparison of performance evaluation are discussed in Sec. 4 followed by concluding remarks in Sec. 5.

2 Materials and Methods

2.1 *Optical Characteristics of Biological Tissue*

In NIR, the light tissue interaction is dominated by the optical properties of tissue, such as absorption, scattering, and so on. The absorption coefficient (μ_a) depends on the wavelength of light used and the concentration of hemoglobin or other constituents. A typical value of absorption coefficient in biological tissue is 0.01 to 0.5 cm^{-1}.[18] Scattering (μ_s) occurs due to the mismatch of the refractive indices between the particles and the surrounding medium; typical scattering coefficient value in tissue is 20 to 200 cm^{-1}.[18] While considering scattering, the anisotropy factor (g) has to be taken into account. It is quantified as the average cosine of the angle of scattering and its value in tissue is 0.8 to 0.98.[18] The scattering coefficient and anisotropy factor produce another parameter called the reduced scattering coefficient that is defined by $(1-g)\mu_s$. Since the scattering coefficient is significantly greater than the absorption coefficient ($\mu_s \gg \mu_a$), the tissue will act as scattering dominant regime, i.e., turbid media. Therefore, light gets diffused in the medium and due to low absorption, NIR light can penetrate more depth compared to that of visible light.

2.2 *Modeling of Photon Propagation and Image Reconstruction*

As tissue acts like turbid media in NIR, the photon propagation can be modeled by diffusion approximation of the radiative transport equation as given by[19]

$$-\nabla\cdot D\nabla\Phi(r,t)+\mu_a\Phi(r,t)+\frac{1}{v}\frac{\partial\Phi(r,t)}{\partial t}=S(r,t), \tag{1}$$

where $\Phi(r,t)$ is the photon fluence rate, $S(r,t)$ is the equivalent isotropic source, and $D=1/3[\mu_a+(1-g)\mu_s]$ is the diffusion coefficient. It should be noted that this approximation requires a highly scattering medium and the distance between source and detector should be much greater than one mean transport path to enhance the number of scattering events. Here, a single isotropic point source and mixed boundary conditions are considered. The mixed or Robin boundary condition can be given as $\Phi+2D\hat{A}\,\hat{n}\cdot(\nabla\Phi)=0$ where $\hat{A}$ is the Fresnel reflection parameter for the medium to air. Considering the tissue refractive index as 1.4,[20] the value of $\hat{A}$ is 2.737. As the analytical solution of Eq. (1) is computationally expensive, numerical solution using finite element method with a Galerkin weighted residual approach[21] is used. Delaunay triangulation with simplex triangular elements is applied for meshing. The total cross-sectional area is divided into around 300 triangular finite elements and the basis functions are those such as the impulse function. In the steady-state form of Eq. (1), the term containing the time derivative of the photon fluence rate is omitted. This solution of $\Phi(r,t)$ when D, μ_a, and $S(r,t)$ are known, is called the forward problem. In image reconstruction, $\Phi(r,t)$ and $S(r,t)$ are known and D and μ_a are estimated, which is called the inverse problem. Since direct inversion of Eq. (1) is not possible and DOT has inherent nonlinearity and ill-posedness, a hybrid approach using both the gradient based method and evolutionary method is implemented here. At first, the reconstruction is done by using a model based iterative method.[22] Starting with some initial guess, the forward problem is solved as described above and predicted measurements are computed. Subsequently, the error between the actual measurements and predicted measurements is minimized iteratively to update the optical parameters. Finally, the parameters are refined using GA and α-trimmed mean filtering. α-trimmed mean filtering is used mainly to reduce the effect of artifacts resulting due to the triangulation procedure used in the finite element solution with a relatively fewer number of source and detectors. The complete block diagram of the method is given in Fig. 1 and described in subsections 2.2.1 and 2.2.2.

2.2.1 *Iterative reconstruction*

Let us consider the forward problem as a function of absorption and scattering coefficients, i.e., $G(\mu_\mathrm{a}, \mu_\mathrm{s}) = M^a$ where $G(\,)$ is the forward function and M^a is the measured detector intensities. Now the coefficients can be considered as the summation of the background value and the perturbation. Hence, the forward problem can be written as $G(\mu_\mathrm{a}^0 + \Delta\mu_\mathrm{a}, \mu_\mathrm{s}^0 + \Delta\mu_\mathrm{s}) = M^a$.

Now applying the Taylor expansion on this function around $(\mu_\mathrm{a}^0, \mu_\mathrm{s}^0)$, and considering up to the first order term, we obtain

$$\begin{aligned} M^a &= G(\mu_\mathrm{a}^0, \mu_\mathrm{s}^0) + G'(\mu_\mathrm{a}^0, \mu_\mathrm{s}^0) \cdot [\Delta\mu_\mathrm{a}, \Delta\mu_\mathrm{s}], \quad \text{or} \\ \Delta M &= J[\Delta\mu_\mathrm{a}, \Delta\mu_\mathrm{s}], \end{aligned} \tag{2}$$

where $\Delta M = M^a - G(\mu_\mathrm{a}^0, \mu_\mathrm{s}^0)$, i.e., the change in intensity due to perturbation in absorption and scattering coefficients and $J = G'(\mu_\mathrm{a}^0, \mu_\mathrm{s}^0)$ is the derivative of the forward problem which can be called Jacobian as well. Jacobian gives the sensitivity of the output measurements corresponding to the variation of absorption and scattering coefficients of each element. Here, the Jacobian has been computed using the perturbation method. The perturbation of the optical coefficients can be obtained by the inverse of the Jacobian multiplied with the change in the detector intensity. However, due to the numerical condition of the Jacobian, the perturbed coefficient values are evaluated iteratively using a least squares method instead of direct matrix inversion. The objective function for least square is

$$\mathrm{Obj} = \|J[\Delta\mu_\mathrm{a}, \Delta\mu_\mathrm{s}] - \Delta M\|^2, \tag{3}$$

where $\|\,\|^2$ denotes the L^2 norm. Using Tikhonov regularization to make the matrix diagonally dominant and invertible, the equation becomes

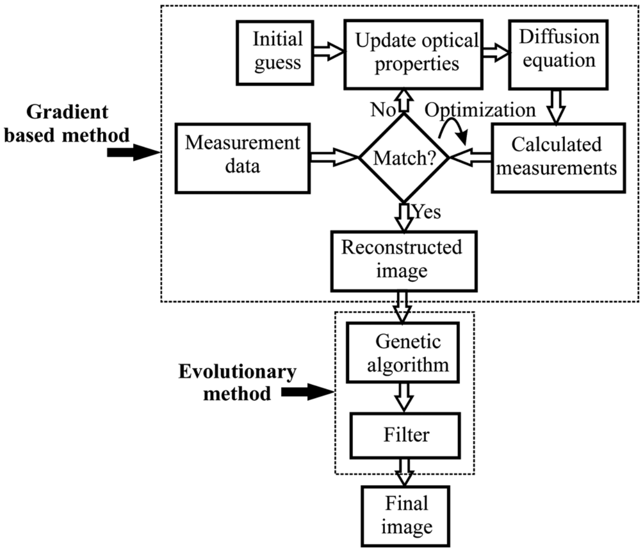

Fig. 1 Block diagram of the proposed methodology of diffuse optical tomography.

$$[J^T J + \lambda I][\Delta\mu_a, \Delta\mu_s] = J^T \Delta M, \tag{4}$$

where λ is the regularization parameter which can be constant or varying. In this case, it is taken as constant. The value of λ is chosen in such a way as to improve the bandwidth of the matrix for efficient computation of the inverse, i.e., to make it diagonally predominant. The value of λ is estimated using the L-curve method.[23] Here, the initial guess values are chosen randomly within the limit of absorption and scattering coefficients and both the parameters are reconstructed. However, only the absorption coefficients are refined in the next stage.

2.2.2 *Coefficient refining using genetic algorithm*

The contrast enhancement is achieved by refining the parameters (absorption coefficients) using GA followed by α-trimmed mean filtering. After model based iterative reconstruction, as depicted above, the reconstructed optical parameters of the sample, having a value higher than a threshold, are refined using GA. The reconstructed absorption coefficient values which are greater than 50% of the maximum values or the top 30% coefficient values, whichever is maximum, are considered for further refinement. GA is a type of evolutionary algorithm which yields an optimal value based on the search population.[24] It is quite successful in the seemingly unknown distribution of a solution in the last few decades. The algorithm uses the principles which are the same as natural genetics. Unlike a conventional search algorithm, GA generally starts with a random set of solutions. Here, GA starts with the results of the iterative reconstruction technique. The basic steps of GA and the selection of parameters have been discussed below.

GA starts with a fixed population of candidate solutions and each of the solutions is evaluated with a fitness function which is the measure of the candidate's potential as a solution. Each individual of the population, called a chromosome, is a binary coded string which is mapped to a scalar value through the fitness function. The fitness function has been computed and minimized to obtain the optimum solution and is finally decoded into a real number of the original feature space. Genetic operators, namely selection or reproduction, cross-over and mutation, are realized to simulate the natural evolution. In selection or reproduction, the fitter solutions are duplicated to replace the bad or less fit solutions in the population while keeping its size constant. Cross-over and mutation are used to generate a new population. In cross-over, two strings are randomly chosen and an exchange of substrings takes place between them to generate a new string. In mutation, the bits of the strings are randomly changed. These three operators are used iteratively until either the fitness function value is under a threshold value or a specific number of iterations has been done.

The fitness function is computed on the mean square error as given by $\theta = \|M_a - f(x')\|^2$ where M^a is the actual detector intensity, $f(x')$ is the forward problem function calculated for x', x' is the optical absorption coefficient assigned to the corresponding chromosome, and $\|\,\|^2$ denotes the L^2 norm. Initially, N number of candidate solutions (chromosome) are generated, which represent the initial absorption coefficients. The input to the algorithm is a point set $P = [A_i | i = 1\!:\!N]$ where parameter vector A_i represents the absorption coefficients assigned to a candidate solution. The initial A_i values are obtained from the least square reconstructed image. The basic GA is depicted below.

```
Algorithm:
Input: Optical parameters from least square
       reconstruction
Output: Refined optical parameters for the final
        reconstructed image
Begin:
  Initialize population size $N$, no. of variables $x$, cross-over rate $P_{co}$, mutation rate $P_{mu}$, desired fitness $\theta$, and n number of $x$-bit chromosome;
  do
    generate m offspring from the parent population considering $P_{co}$, $P_{mu}$
    solve forward problem for each offspring
    compute the fitness value of each of them and rank accordingly (i.e., the smallest fitness corresponds to rank 1)
    select first $N$ chromosomes
  end until any chromosome's fitness value exceeds the desired fitness
  chromosome with the highest rank is the optimal solution
End
```

Here, the parameters of GA are the population size, mutation rate, lower and upper bounds of feature values, and so on. The population size depends on the number of variables and it is taken as about four times the number of variables. Since least square is stuck near some local or global minima, a high-mutation rate is chosen which ensures 80% of the old population will migrate to the new population. The lower bound is the minimum value of the reconstructed absorption coefficient by least square and the upper bound is considered a very high value of the absorption coefficient (a typical value of 0.8 mm^{-1}). The iteration of these steps will continue until either the fitness function is steady or a particular number of iterations is reached. The maximum allowable number of iterations is 500 and the limit of cumulative change in the fitness function is 0.00001.

Finally, α-trimmed mean filtering of the reconstructed image is done. Due to the small number of the source-detector and quantization effects, the shape of the inclusion is not smooth. Therefore, α-trimmed mean filtering is used for smoothing the image. Based on order statistics, the filter varies between mean and median according to the value of alpha (α). Depending upon the mask size, the surrounding neighborhood pixel values are sorted in ascending order and removing the first ($\alpha/2$) and last ($\alpha/2$) values, the mean is taken for the remaining values. The filtered output is the final reconstructed DOT image.

3 Experimental Setup and Sample Preparation

The phantom used in the experiment is cylindrical in shape with dimensions 25 mm × 45 mm (radius × height with center at origin) bearing double inclusions. The background material was composed of 2% agarose gel (Cat no. A9539, Sigma Aldrich) containing 2:1 (v/v) agarose and cornstarch. An appropriate amount of agarose and distilled water was mixed. The mixture was heated in order to dissolve the agarose and obtain a transparent liquid followed by addition of an appropriate amount of cornstarch. Subsequently, the solution was poured into a cylindrical mold and allowed to cool. After that, the mold design allowed the final cooled solidified phantom to bear small holes [Fig. 2(a)]. Finally, a mixture of 1:1 (v/v) blue India ink and glycerin was poured into the holes to mimic optically high-absorptive objects. The inclusions are of radius 4 mm with the center at (0, 10) mm and of radius 3.5 mm with the center at (6, −10) mm. Figure 2(a) represents the sample under study. The absorption coefficient of the ink and glycerin mixture was determined using a spectrophotometer (Jasco V630 spectrophotometer). At the working wavelength, i.e., 680 nm, the average absorption coefficient of the ink and glycerin mixture was found to be 0.52 mm^{-1}. The experimentally estimated absorption and reduced scattering coefficients of agarose were 0.056 and 5 mm^{-1}, respectively.

The overall experimental setup for data acquisition has been depicted in Fig. 2(b). It can be divided into two modules; illumination module and detection module. The main component of the illumination module is a semiconductor laser operating at 680 nm. The power of the laser source is kept at around 2 mW, which is less than the maximum permissible exposure limit. The laser, coupled with a multimode plastic fiber, illuminates the sample continuously at different source locations by rotating it around the sample along the xy-plane. The sample is kept in a cylindrical chamber having holes on the outer surface at different xy-planes. Multimode plastic fibers are placed through these holes to measure the light intensity at the boundary. These detector fibers are attached to a disk according to their relative position and data acquisition is performed using a CCD camera. A set of close-up lenses with focal length of 37.5 mm is placed in front of the camera lens to focus the incoming light more closely and the intensity values are obtained from

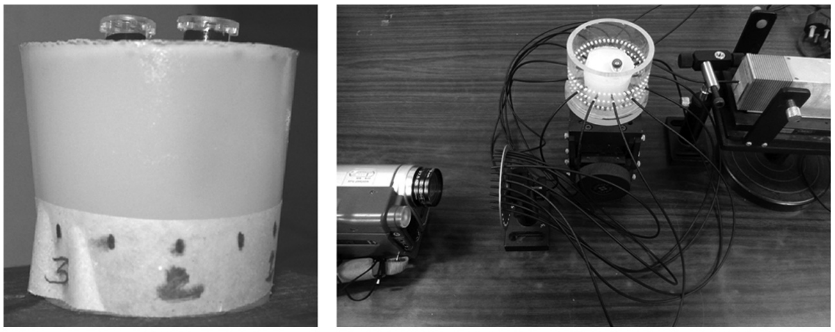
(a) (b)

Fig. 2 (a) The agarose sample and (b) experimental setup for data acquisition.

the pixel intensity of the corresponding frame. The intensity of the source is adjusted so that the maximum and minimum detector intensities are within the dynamic range of the CCD. The source and detector nodes are placed alternately along the circumference of the imaging plane with equal spacing. Here, the CW mode of measurement and a CCD camera are used to make the system low-cost and portable. The source node position is scanned over the surface and measurement is repeated to acquire a set of data. Finally, the average of three sets of data is considered to reduce the zero-mean noise present in the measurement. A total of seven sources and seven detectors were used in the experiment hence, 49 measurement data for the reconstruction of the cross section were obtained.

4 Results and Discussions

4.1 *Simulated Targets*

Circular numerical phantoms having different inclusions are considered for this study. A circular phantom of radius 80 mm and center at (0, 0) mm having absorption and reduced scattering coefficients of 0.025 and 2 mm^{-1}, respectively, has been used as background. In first case, the phantom has a single inclusion of radius 20 mm with center at (20, −20) mm. The absorption coefficient of the inclusion is 0.2 mm^{-1}. A total of eight source nodes and 18 detector nodes have been considered over the boundary for measurement purposes. The second phantom has three inclusions of radius 15 mm with centers at (0, 40) mm, (40, 0) mm, and $(-30, -30)$ mm, respectively. All three inclusions have absorption coefficients of 0.5 mm^{-1} and have 16 source nodes and 16 detector nodes placed alternately on the boundary. The third phantom has two inclusions; one inclusion is of radius 12.5 mm with the center at $(-25, -25)$ mm and the absorption coefficient is 0.2 mm^{-1}. The other inclusion is elliptical with a major axis of 40 mm, minor axis of 25 mm, and center is at (28, 28) mm with an absorption coefficient of 0.2 mm^{-1}. Sixteen source and detector nodes are considered alternately over the boundary. The fourth phantom has two inclusions of radius 15 mm with centers at (22, −22) mm and (−28, 34) mm, respectively. The two inclusions have absorption coefficients of 0.2 and 0.3 mm^{-1}, respectively, and have 16 source nodes and 16 detector nodes placed alternately on the boundary. The fifth phantom is similar to the agarose phantom used in the experimental study. The radius is 25 mm with background absorption and a reduced scattering coefficient of 0.056 and 5 mm^{-1}, respectively. One inclusion is of radius 4 mm with the center at (0, 10) mm and the other inclusion is of radius 3.5 mm with the center at (6, −10) mm. The absorption coefficient of inclusions is 0.52 mm^{-1} and a total of seven source and seven detectors are placed alternately in an equispaced fashion along the boundary. All five phantoms are shown in Figs. 3(a)–3(e). The reason behind considering a circular phantom is to make the algorithm direction invariant. Also, the scattering coefficient is considered as known and constant in this study because the scattering coefficient of biological tissue is known to remain within a range and does not change with different tissue components. However, it has been checked that a change in the scattering coefficient may affect the reconstruction of the absorption coefficient to some extent.

The boundary intensity measurement data for the numerical phantoms are generated by solving the forward problem. The steady state diffusion equation is solved by using the Galerkin weighted residual method as discussed in Sec. 2.2. The source light is incident at a source node and light intensities reemitted from the surface are measured at the detector nodes. Subsequently, the incident position of the source light is scanned over the surface and the measurement of light intensity is repeated to acquire a set of measurement data. This measurement data is used to reconstruct the optical parameters of the phantoms. The overall programming has been carried out in MATLAB® environment (version 7.8.0) and the solution details of the forward problem are given in our earlier paper.[25]

The optical absorption coefficients of the numerical phantoms have been reconstructed using a model based iterative reconstruction and GA as described in Sec. 2.2. At first, model based iterative reconstruction using the least square method is used to update the coefficients. The typical value of the regularized parameter (λ) is 6×10^{-6}. The reconstruction of the absorption coefficients of the first phantom using a regularized nonlinear least square has been shown in Fig. 4(b), whereas the actual absorption coefficient map is shown in Fig. 4(a). It is

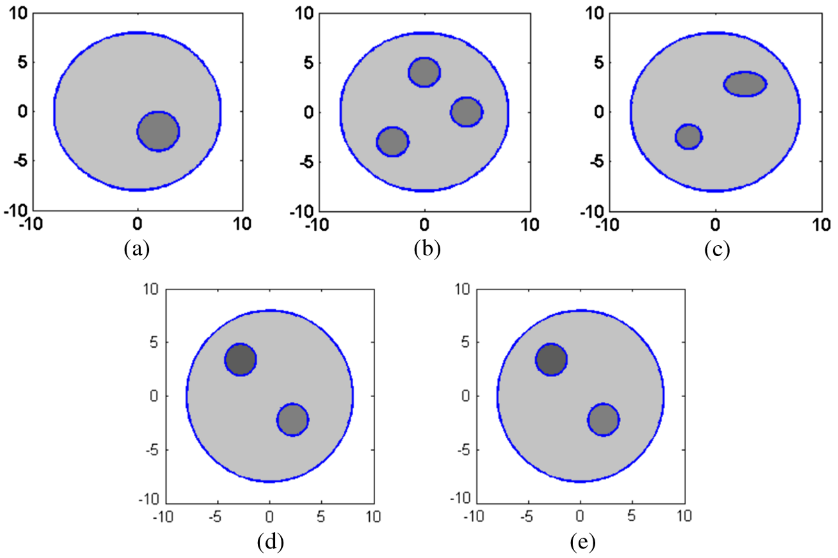

Fig. 3 (a-e) Cross-sectional view of all five numerical phantoms.

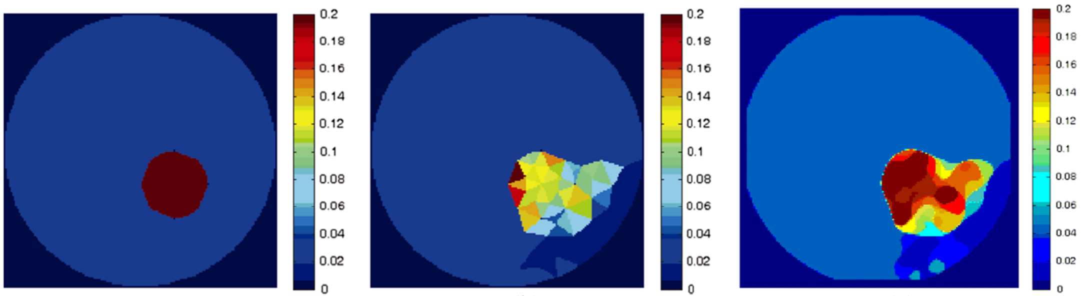

(a) (b) (c)

Fig. 4 (a) Actual absorption coefficient map of first phantom and its reconstruction using (b) least square method and (c) proposed method.

evident from Figs. 4(a) and 4(b) that though the spatial accuracy is satisfactory, the contrast is lower than that of the original. To improve the contrast of the inclusion, the parameters are further refined using GA. This reduces the search domain of GA and thus the computational complexity, achieving a better solution. The other parameter values of GA are given below. The population size is 150. After 25 generations, the migration of individuals will occur and 80% of the old population will migrate to the new population. The maximum number of iterations is 500 and the tolerance for the cumulative change in the fitness function is 0.00001. A lower bound of 0.025 mm^{-1} and an upper bound of 0.8 mm^{-1} are used as constraints in GA. For α-trimmed mean filtering, the mask size is (5×5) pixels and the value of α is 20. The final reconstructed absorption coefficient cross-section is given in Fig. 4(c). Although the size of the inclusion is a little bigger than that of the original one, the contrast has been improved from that of the least square reconstruction. The quantitative reconstruction accuracy is discussed in Sec. 4.3.

Subsequently, the optical properties of the second numerical phantom are reconstructed when having multiple inclusions. The actual and the least square reconstructed absorption coefficients are shown in Figs. 5(a) and 5(b), respectively. The locations of the inclusions are detected accurately, but the contrast is lower than those of the actual ones. Therefore, to minimize the total mean square error, the inclusions have more area than the actual inclusions. Then the coefficients are refined using GA with the same parameter values. Figure 5(c) depicts the final reconstructed absorption coefficients with improved contrast.

Similarly, the optical absorption coefficients of the third phantom are reconstructed as shown in Fig. 6. Figure 6(a) is the actual phantom, whereas Figs. 6(b) and 6(c) are the reconstructed image using the least square and least square with GA, respectively. Although, the spatial accuracy is satisfactory in Fig. 6(b), the contrast is very low. On the other hand, in Fig. 6(c), both the spatial accuracy and contrast are improved. Since the least square reconstructed image is used as the initial condition for GA, the presence of noise is less. Therefore, the

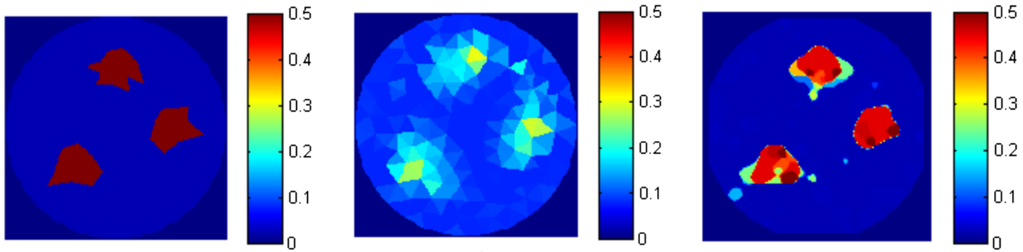

(a) (b) (c)

Fig. 5 (a) Actual absorption coefficient map of second phantom and its reconstruction using (b) least square method and (c) proposed method.

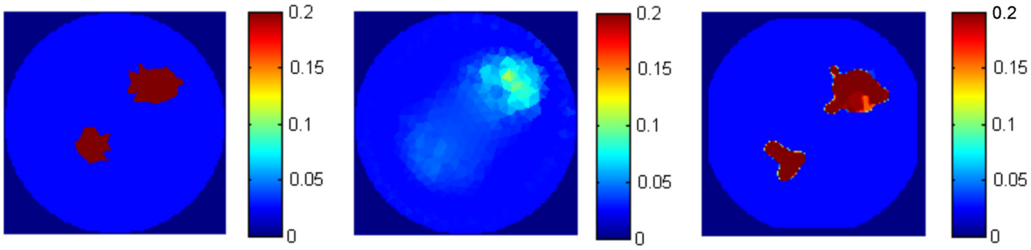

(a) (b) (c)

Fig. 6 (a) Actual absorption coefficient map of third phantom and its reconstruction using (b) least square method and (c) proposed method.

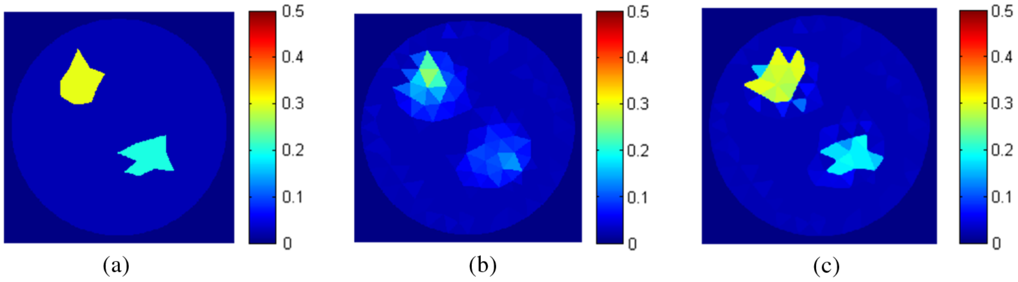

Fig. 7 (a) Actual absorption coefficient map of fourth phantom and its reconstruction using (b) least square method and (c) proposed method.

outcome of GA is not affected by noise. As GA is susceptible to noise, knowledge of the noise model is required for actual convergence. However, since the initial condition has less noise and it is not random, GA is immune to noise here.

The optical absorption coefficients of the fourth phantom are reconstructed as shown in Fig. 7. Figure 7(a) is the actual phantom, whereas Figs. 7(b) and 7(c) are the reconstructed image using least square and least square with GA, respectively. In Fig. 7(b), the contrast is very low and the size of the inclusion is large, whereas the contrast and structural similarity are improved in Fig. 7(c).

The optical absorption coefficients of the fifth phantom are reconstructed as shown in Fig. 8. Figure 8(a) is the actual phantom, whereas Figs. 8(b) and 8(c) are the reconstructed image using least square and least square with GA, respectively. It is evident from Fig. 8(b) that the contrast is very low, whereas the contrast is improved in Fig. 8(c).

4.2 *Phantom Experiment*

A phantom experiment was performed to validate the proposed method. The details of the experimental setup and phantom preparation were already discussed in Sec. 3. The reconstruction result for the experimental data is shown in Fig. 9. The actual absorption cross-section of the experimental phantom is shown in Fig. 9(a), with two inclusions. The least square reconstructed absorption profile is shown in Fig. 9(b). It is evident from Fig. 9(b) that along with the inclusion locations, a few boundary elements also have high-absorption coefficients. This may be due to various errors in the experimental data like measurement noise, a limited number of source and detectors, the effect of ambient light, and so on. The coefficients are selected as described above and are denoted by the area enclosed by white curves in Fig. 9(c). The selected coefficients are refined using GA followed by α-trimmed mean filtering. The final reconstructed absorption profile is shown in Fig. 9(d). It is obvious in Fig. 9(d) that after GA and α-trimmed mean filtering, the high-absorption discrete elements on the boundary are removed. The detected inclusion contours (white lines) are shown in Fig. 9(e) and are qualitatively compared with the actual inclusions. The blue and cyan colored blobs are the actual inclusions. To quantify the quality of the reconstruction and compare them with other methods, quantitative performance analysis has been carried out as discussed in Sec. 4.4.

The proposed algorithm is validated with homogeneous numerical simulations as well as an agarose phantom. The reconstructed absorption coefficient map for the numerical and experimental phantoms are shown in Figs. 10(b) and 10(d), respectively, whereas the actual absorption profiles for the same are shown in Figs. 10(a) and 10(c), respectively. It is evident from Figs. 10(b) and 10(d) that the proposed system can also correctly reconstruct media with no inclusion as well. Some small fluctuations are noticed in the reconstructed figures of Figs. 10(b) and 10(d), however, it is worth mentioning that the maximum of the scales in these figures is 0.1 and the fluctuations are of magnitudes around 0.06, which is very close to the background values of 0.056.

4.3 *Clinical Application of Diffuse Optical Tomography in Finger Joint Imaging*

In recent years, optical imaging has been explored for detecting OA.[3,26,27] In previous studies, it has been shown that the absorption coefficients of a joint cavity increased in the case of OA compared to healthy people. Therefore, we have studied the DIP joint of human fingers of different age-groups to illustrate the clinical applicability of the proposed method. This study was performed under ethical guidelines of the institutional ethical committee. In our study, imaging was done on the right index DIP joint of three healthy subjects. The first and second healthy volunteers are males of age 27 years (case 1) and 52 years (case 2), respectively, and the third healthy volunteer

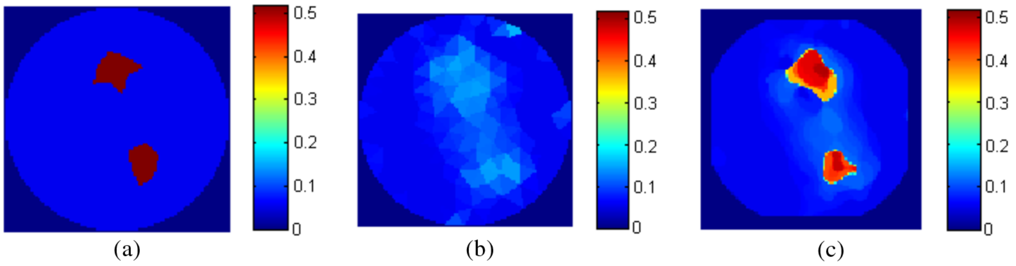

Fig. 8 (a) Actual absorption coefficient map of fifth phantom and its reconstruction using (b) least square method and (c) proposed method.

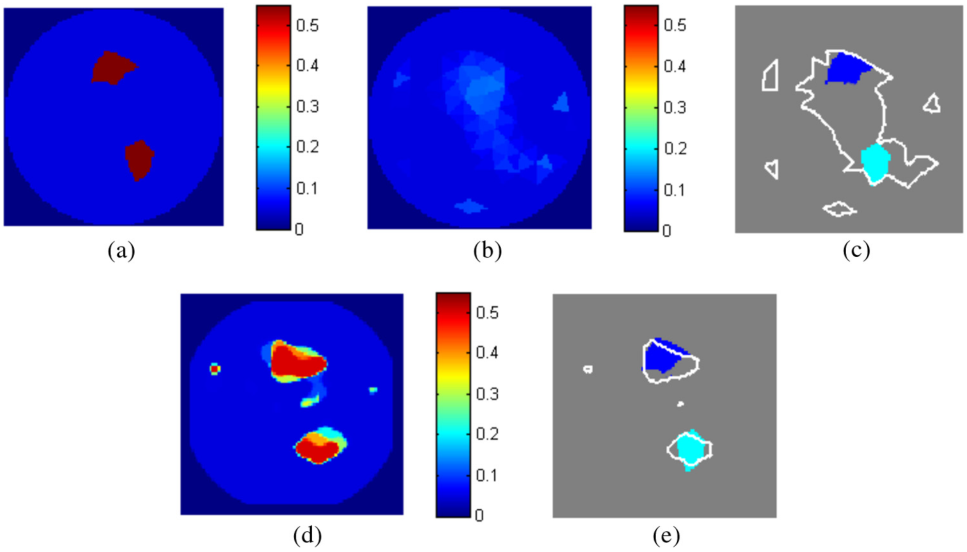

Fig. 9 (a) Actual absorption coefficient map of agarose phantom and its reconstruction using (b) least square method and (d) least square with genetic algorithm (proposed hybrid method). (c) The initial search space for genetic algorithm (GA) denoted by the area enclosed by white curves and (e) the final outcome of GA for reconstructed absorption coefficients.

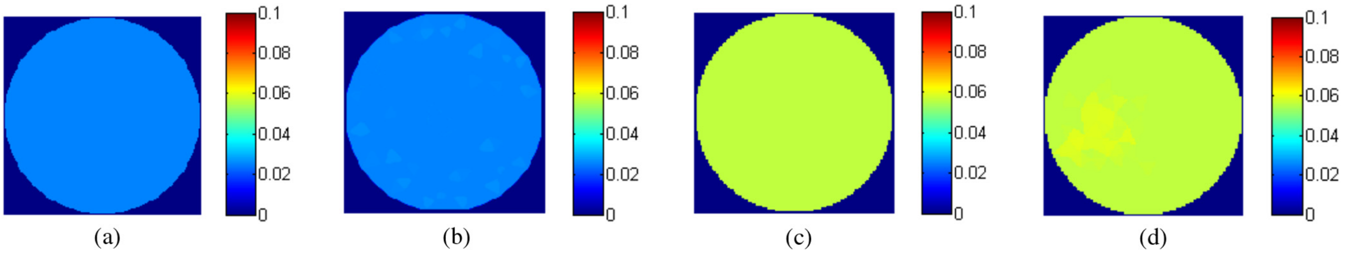

Fig. 10 (a) Actual absorption coefficient map of homogeneous (a) numerical and (c) agarose phantom and reconstructed absorption coefficient of (b) numerical and (d) agarose phantom using proposed method.

is female of age 29 years (case 3). None of the subjects had ever been diagnosed with OA or experienced symptoms of OA. The third volunteer rarely experienced morning stiffness in joints with no OA diagnosis. The finger joint is illuminated with a semiconductor CW laser of 680 nm (2-mW power) and the intensity at the boundary is measured using a CCD as described in Sec. 3. A total of seven detectors and one source are placed at equal gaps on the boundary of the DIP joint and the whole source detector setup is rotated by 90 deg to obtain measurements for four different source locations. The absorption profiles of the transverse section through the DIP joint of the three volunteers have been reconstructed using iterative reconstruction only and the proposed method. Figures 11(a)–11(c) illustrate the reconstructed absorption coefficients for cases a, b, and c, respectively, using the iterative reconstruction method. The reconstructed absorption coefficients for cases a, b, and c using the proposed method are portrayed in Figs. 11(d)–11(f). It is evident from Figs. 11(d)–11(f) that all three images exhibit similar patterns of absorption coefficients. The center of the joint is like a void region with a low-absorption coefficient where NIR absorption is minimal. A nearly annular region of high absorption is surrounding the center cavity. The absorption coefficient of this annular region increases with degradation in the joint from normal to OA. Since the condition of the joint degrades with age, the thickness of annular region is greater in case 2 than that in case 1. In the case of the third volunteer, the absorption coefficient and thickness of the annular region are greater than that in case 1. These results are in agreement with similar results available in the literature.[26] Therefore, the absorption coefficient profile of a DIP joint has a direct impact on the monitoring of joint condition as well as diagnosis/progression of OA.

4.4 *Performance Evaluation*

To assess the performance of the proposed method, different performance metrics have been used as described below.[28] Mean square error is calculated as $\mathrm{MSE} = \underset{i \in \Omega}{\text{mean}} \{[\mu_a^t(i) - \mu_a^e(i)]^2\}$ where μ_a^t and μ_a^e are the target/actual and estimated/reconstructed absorption coefficients, respectively. This can be normalized as

$$n\mathrm{RMSE} = \left(\sqrt{\underset{i \in \Omega}{\text{mean}} \quad \{[\mu_a^t(i) - \mu_a^e(i)]^2\}} \right) / (\mu_a^{\max} - \mu_a^{\min}), \tag{5}$$

where $\mu_a^{\max}, \mu_a^{\min}$ are the maximum and minimum values of the reconstructed absorption coefficient, respectively. Object

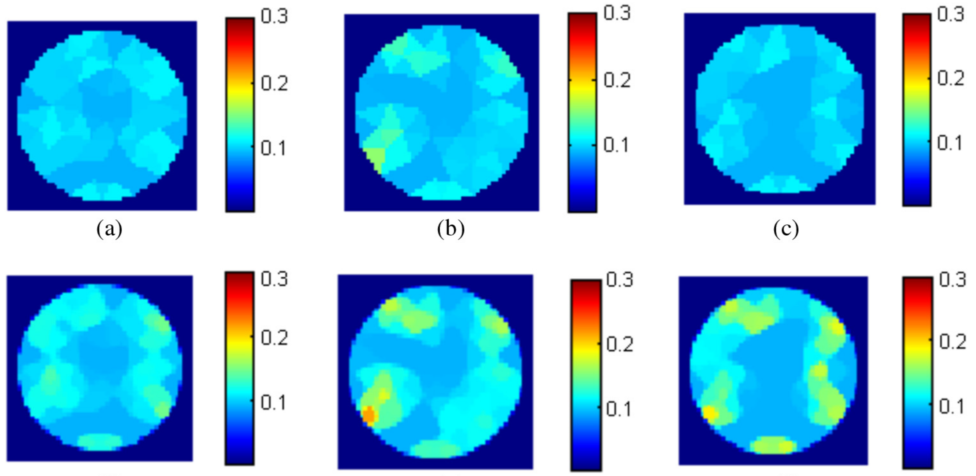

(a) (b) (c)

(d) (e) (f)

Fig. 11 The absorption profile of transverse section of right index distal interphalangeal joint of (a) and (d) case 1 (male, 27 years), (b) and (e) case 2 (male, 52 years) and (c) and (f) case 3 (female, 29 years). First, the images are reconstructed using iterative reconstruction only (a)–(c) and then the proposed hybrid method is used (d)–(f).

centroid error (OCE) denotes the spatial variation of the centroid of the reconstructed inclusion with respect to the actual inclusion location. Primarily, the inclusion threshold is set as 50% of the maximum value of the reconstructed coefficient and the centroid is calculated as the weighted average with the reconstructed absorption coefficients as the weights. OCE is the difference between the calculated centroid $(r_{\mathrm{est},I})$ and the actual centroid $(r_{\mathrm{true},I})$. The observed contrast can be defined as $C_\mathrm{o} = 20\log_{10}(\Delta\hat{\mu}_{\mathrm{a},I}/\Delta\hat{\mu}_{\mathrm{a},B})$ where $\Delta\hat{\mu}_{\mathrm{a},I}$ and $\Delta\hat{\mu}_{\mathrm{a},B}$ are the average relative absorption coefficients of the inclusion and background of the same area, respectively. This is computed as a percentage of the actual contrast value. These three measures have been computed for the proposed method for simulation as well as experimental data and the results are compared with the results given in Ref. 28. All the values are tabulated in Table 1 and we have taken the best obtained results for each algorithm. The performance values for the first four methods are taken from Ref. 28 and are based on numerical phantom. It is evident from Table 1 that OCE has improved significantly from that of the other methods. The value of C_o is 98.4% in simulation and 90.7% in the experimental data using the proposed method. On the other hand, the MSE is not improved from the existing algorithm as they are nearly same values. However, the MSE is greater for experimental data than that of the simulation. This is due to the presence of different noise in the experimental data, as explained earlier. The value of nRMSE is 0.494.

Table 1 Comparison of performance of the proposed method with other existing methods.

		Performance measures		
Algorithm		MSE	OCE (mm)	C_o
Algebraic reconstruction technique[28]		0.001	2.5	–
Simultaneous iterative reconstruction technique[28]		0.0005	1.2	–
Truncated singular value decomposition[28]		0.0006	1.1	–
Truncated conjugate gradient[28]		0.0005	0.99	–
Proposed method	Simulation	0.0009	0.01 to 0.22	98.4%
	Experimental	0.0059	0.03 to 1.03	90.7%

These values are also compared with,[15] another GA based reconstruction method. In Ref. 15, the mean OCE is within 0.6 mm for noise free data and within 3 mm for noisy data with a signal to noise ratio of 100. In our proposed method, OCE is within 0.22 mm in simulation (i.e., noise free) and within 1.03 mm in the experiment (may have noise). It is evident that OCE has improved in our proposed method over that of Ref. 15. Also, the error in the reconstructed absorption coefficient is 0.037 cm^{-1} (for noisy data) in Ref. 15 whereas the same is 0.031 cm^{-1} for the experimental data in the present study. These significant improvements in the reconstruction using the proposed algorithm illustrate its potential to enhance the contrast of the reconstructed image. The reconstruction accuracy of the proposed algorithm is compared with that of TOAST software as used in Ref. 29. In Ref. 29, the error in distance between two inclusions is 0.9 mm and the same in the radii of inclusions are in between 0.8 and 2.9 mm. The mesh of the phantom consists of 13,174 nodes and 78,113 elements [three-dimensional (3-D)] whereas the same for the mouse measurement is 13,452 nodes and 80,361 elements (3-D). In the present study, the mess consists of 150 nodes and 256 elements (two-dimensional). The OCE is 0.01 to 1.03 mm in our proposed method which is comparable with the performance of Ref. 29. Hence, the proposed method can be a good candidate for diagnostic imaging in clinical applications.

5 Conclusions

In this study, a hybrid method using both regularized least square and GA is proposed to improve the contrast of reconstructed images in DOT which increases the sensitivity of the diagnostics imaging to a great extent. The model based iterative reconstruction technique using least square method gives a reconstructed image with low contrast. The GA based estimation refines the reconstructed optical parameters to improve the contrast of the reconstructed image. Different performance measures are used to compare the proposed method with the existing algebraic and subspace reconstruction techniques. It is shown that using the proposed method, the OCE is significantly reduced whereas the mean square error is almost the same with respect to the existing methods. The OCE is 0.01 to 0.22 mm in simulation and 0.03 to 1.03 mm in the experimental data. The contrast of the reconstructed image is 98.4% in simulation and 90.7% in the experimental data. These performance metrics show the accuracy of reconstruction of the contrast or optical parameters which are comparable with that of pulsed DOT or frequency domain DOT facilitating functional imaging using DOT. The proposed method has been validated experimentally on tissue-like phantoms. Usage of an ordinary CCD camera, low cost CW laser, and a small number of low cost plastic fibers as collection optics reduce the overall cost of the instrument and make it portable. These results reinforce its potential to be used for diagnostic DOT imaging. An example of finger joint imaging for OA diagnosis is illustrated as well. Apart from diagnostic imaging, this method can also be used for concentration measurement of a region of interest in a turbid media.

References

1. M. Schweiger and S. R. Arridge, "Optical tomographic reconstruction in a complex head model using a priori region boundary," *Phys. Med. Biol.* **44**, 2703–2721 (1999).
2. B. W. Pogue et al., "Instrumentation and design of a frequency domain diffuse optical tomography imager for breast cancer detection," *Opt. Express* **1**, 391–403 (1997).
3. U. J. Netz et al., "Optical tomography in the diagnosis of rheumatoid arthritis-method and implementation," *Med. Laser Appl.* **22**, 15–22 (2007).
4. M. Schweiger, S. R. Arridge, and D. T. Delpy, "Application of the finite element method for the forward and inverse models in optical tomography," *J. Math. Imaging Vision* **3**, 263–283 (1993).
5. S. A. Arridge and J. C. Schotland, "Optical tomography: forward and inverse problems," *Inverse Probl.* **25**, 123010 (2009).
6. M. Suzen, A. Giannoula, and T. Durduran, "Compressed sensing in DOT," *Opt. Express* **18**, 23676 (2010).
7. O. Lee et al., "Diffuse optical tomography using generalized music algorithm," in *Proc. of Int. Symp. on Biomedical Imaging*, Chicago, Illinois (2011).
8. Q. Wu, Z. Qian, and Y. Gu, "An optimization algorithm to inverse problem in 2-D optical computed tomography by BP neural network," in *Proc. of Int. Symp. on Biophotonics, Nanophotonics and Metamaterials*, Hangzhou, China (2006).
9. C. B. Shaw and P. K. Yalavarthy, "Effective contrast recovery in rapid dynamic near-infrared diffuse optical tomography using l1-norm-based linear image reconstruction method," *J. Biomed. Opt.* **17**(8), 086009 (2012).
10. C. B. Shaw and P. K. Yalavarthy, "Performance evaluation of typical approximation algorithms for nonconvex ℓ_p-minimization in diffuse optical tomography," *J. Opt. Soc. Am. A* **31**(4), 852–862 (2014).
11. J. Prakash et al., "Model-resolution-based basis pursuit deconvolution improves diffuse optical tomographic imaging," *IEEE Trans. Med. Imaging* **33**(4), 891–901 (2014).
12. A. H. Hielscher, A. D. Klose, and J. Beuthan, "Evolution strategies for optical tomographic characterization of homogeneous media," *Opt. Express* **7**(13), 507–518 (2000).
13. A. D. Klose and A. H. Hielscher, "An approach for diffuse optical tomography combining evolution strategies and gradient techniques," *Proc. SPIE* **4250**, 11–19 (2001).
14. M. L. Flexman et al., "A wireless handheld probe with spectrally constrained evolution strategies for diffuse optical imaging of tissue," *Re. Sci. Instrum.* **83**(3), 033108 (2012).
15. Q. Zhao et al., "Reconstruction in diffuse optical tomography using genetic algorithm," *OSA Biomed.* (2010).
16. A. R. Sethi, H. S. Patel, and A. Srivastava, "Quantitative imaging of inhomogeneities in turbid medium using diffuse optical tomography: a genetic algorithm based approach," *Proc. SPIE* **8578**, 85781A (2013).
17. B. Tavakoli and Q. Zhu, "Two-step reconstruction method using global optimization and conjugate gradient for ultrasound-guided diffuse optical tomography," *J. Biomed. Opt.* **18**(1), 016006 (2013).
18. D. A. Boas, C. Pitris, and N. Ramanujam, *Handbook of Biomedical Optics*, CRC Press, Boca Raton, Florida (2011).
19. E. W. Larsen and J. B. Keller, "Asymptotic solution of neutron-transport problems for small mean free paths," *J. Math. Phys.* **15**, 75–81 (1974).
20. F. P. Bolin et al., "Refractive index of some mammalian tissues using a fiber optic cladding method," *Appl. Opt.* **28**, 2297–2302 (1989).
21. J. N. Reddy, *An Introduction to the Finite Element Method*, Tata Macgraw Hill, New Delhi, India (1993).
22. F. S. Azar and X. Intes, *Translational Multimodality Optical Imaging*, Artech House, Norwood, Massachusetts (2008).
23. P. J. Mc Carthy, "Direct analytic model of the L-curve for Tikhonov regularization parameter selection," *Inverse Probl.* **19**, 643–663 (2003).
24. D. E. Goldberg, *Genetic Algorithms in Search, Optimization, and Machine Learning*, Addison Wesley Professional Publishers, Boston, Massachusetts (1989).
25. R. Patra and P. K. Dutta, "Improved DOT reconstruction by estimating the inclusion location using artificial neural network," *Proc. SPIE* **8668**, 86684C (2013).
26. J. M. Lasker et al., "Dynamic optical imaging of vascular and metabolic reactivity in rheumatoid joints," *J. Biomed. Opt.* **12**(5), 052001 (2007).
27. A.H. Hielscher et al., "Frequency-domain optical tomographic imaging of arthritic finger joints," *IEEE Trans. Med. Imaging* **30**(10), 1725–1736 (2011).
28. R. J. Gaudette et al., "A comparison study of linear reconstruction techniques for diffuse optical tomographic imaging of absorption coefficient," *Phys. Med. Biol.* **45**, 1051–70 (2000).
29. N. Ducros et al., "Fluorescence molecular tomography of an animal model using structured light rotating view acquisition," *J. Biomed. Opt.* **18**(2), 020503 (2013).

Rusha Patra received her Bachelor of Electrical Engineering degree from Jadavpur University, Kolkata, in 2008 and her MTech degree in medical imaging and image analysis from the Indian Institute of Technology (IIT) Kharagpur in 2010. She was recipient of Institute Silver medal for being best outgoing postgraduate student of her department. Currently, she is a research scholar in the Department of Electrical Engineering at IIT Kharagpur. Her current research interests include optical imaging and solution of inverse problems.

Pranab K. Dutta received his BE and ME degrees in electrical engineering from the University of Calcutta, Kolkata, India, in 1984 and 1986, respectively, and his PhD in electrical engineering from the Department of Electrical Engineering, IIT Kharagpur, in 1992. Currently, he is a professor in the Department of Electrical Engineering with IIT Kharagpur. His principal research interests include signal processing, optoelectronics and optical imaging, and biomedical image processing.